ELSEVIER

Polymer Vol. 37 No. 14, pp. 2887–2902, 1996

0032-3861/96/$15.00+0.00

polymer papers

Diffusion of small-molecule penetrants in polyethylene: free volume and morphology

M. Hedenqvist, A. Angelstok, L. Edsberg*, P. T. Larsson† and U. W. Gedde‡
Department of Polymer Technology, Royal Institute of Technology, S-100 44 Stockholm, Sweden
(Received 28 August 1995)

Based on desorption and permeation measurements, the diffusivity and solubility of n-hexane and oxygen have been obtained for a wide range of linear and branched polyethylenes (PEs) with crystallinities between 40 and 97% and mass-average molar masses between 10^3 and 10^6 g mol^{-1}. The morphology and contents of crystal core (CC), crystal-core-like interfacial (I_{CC}), liquid-like interfacial (I_L) and liquid (L) components were assessed by transmission electron microscopy, Raman spectroscopy, ^{13}C cross-polarization/magic-angle spinning nuclear magnetic resonance spectroscopy, differential scanning calorimetry, density measurements and small-angle light scattering. The penetrant solubility in the non-crystalline phases increased with increasing concentration of chain ends and chain branches. This effect was masked at certain crystallinities by the constraining effect of the crystallites. The diffusivity selectivity of oxygen over n-hexane increased strongly with increasing crystallinity and decreasing non-crystalline layer thickness, demonstrating that the crystal-induced constraint on the non-crystalline chains more efficiently retards the diffusion of larger molecules. The fractional free volume of the non-crystalline components decreased strongly with increasing crystallinity in the low-crystallinity range (<60%), above which it remained practically constant. The latter is because the constraining effect of the crystals is compensated for by the plasticizing effect of the chain ends, which leads to a constant free volume in this crystallinity range. A model, based on the Cohen–Turnbull–Fujita (CTF) model, considering the polymers to consist of four components, CC, I_{CC}, I_L and L, was applied to the diffusivity data. The branched PEs and the majority of the linear PEs could be described by the modified CTF model. However, the lowest-molar-mass linear PEs exhibited a considerably larger interfacial free volume than the other samples. Real-time Raman spectroscopy on CCl_4-swollen samples showed that the changes in the CC and I_{CC} contents during sorption were only small. Copyright © 1996 Elsevier Science Ltd.

(Keywords: polyethylene; solubility; diffusivity)

INTRODUCTION

The diffusion of penetrants in semicrystalline polymers occurs almost exclusively through the amorphous phase. The crystals are generally considered to be impenetrable for all non-reactive molecules, although the smallest gases, e.g. He, may penetrate the crystalline component[1]. The crystals constitute obstacles to the transport of penetrants through the system, causing an extension of the diffusion path. The related so-called 'geometrical impedance' is conventionally expressed by a tortuosity factor in the model of Michaels and Bixler[2] or by the detour factor used by Peterlin[3]. The segmental mobility of the amorphous component is strongly reduced by the 'constraining' crystallites. There is also a gathering of chain defects, i.e. chain ends and chain branches, in the amorphous component, which essentially causes an increase of the free volume[4].

Doolittle-type free-volume equations have been applied to describe the diffusivity in several solute–polymer systems[5]. The theory of Turnbull and Cohen[6,7] applied to liquids and later to polymers by Fujita[8] has been utilized to model solute diffusion in semicrystalline polymers above their glass transition temperature, e.g. diffusion in polyethylene (PE) at room temperature. The Cohen–Turnbull–Fujita (CTF) model successfully describes the concentration dependence of the diffusivity on the assumption that the fractional free volume of the swollen polymer is the sum of the fractional free volumes of pure polymer and pure solute (this is not a necessary condition in all CTF models[5]). A drawback of the CTF model is that it uses some parameters that have not been given a strict physical interpretation[4,9].

PE has hitherto been treated as a two-component polymer consisting of an inaccessible impermeable crystalline component and a penetrable non-crystalline component. N.m.r. and Raman data on PE, however, indicated the presence of a third or even a fourth component, which have been suggested to be of a disordered but anisotropic nature[10]. These microstructural observations raise questions concerning solubility and diffusivity in PE: Does the penetrant enter these intermediate components? What is the intrinsic 'diffusivity' in this zone? This is analysed here by considering PE as a four-component material[10] consisting of a crystal core (CC) with no diffusivity and

* Present address: Department of Numerical Analysis and Computing Science, Royal Institute of Technology, S-100 44 Stockholm, Sweden
† Present address: STFI, Box 5604, S-114 86 Stockholm, Sweden
‡ To whom correspondence should be addressed

solubility for medium-sized and larger molecules, a liquid-like component (L) resembling the properties of the fully amorphous polymer, and two components of intermediate conformational order and mobility. The intermediate components are denoted crystal-core-like (I_{CC}) and liquid-like (I_L) interphase components. This paper presents data from the desorption of n-hexane and the permeation of oxygen in/through a series of linear and branched PEs. These experiments were selected to avoid the complication of having adjustable parameters in the equations describing the boundary conditions. The variation in mass crystallinity and molar mass among the studied PEs was extensive: 40–97% for crystallinity and 10^3–10^6 g mol^{-1} for molar mass. Most of the linear PEs consisted of narrow-molar-mass fractions with uniformity indices between 1.1 and 1.3. The first part of the paper presents results from assessments of phase structure (crystallinity and contents of CC, I_{CC}, I_L and L components) and morphology (crystal thickness and width, and thickness of the non-crystalline interlayer). The second part presents data on solubility and diffusivity interpreted according to a modified CTF model including, in addition to the conventional crystalline and liquid-like components, a third interfacial component I ($I_{CC} + I_L$). The available extensive morphological data make it possible to separate the influence of geometrical impedance from the constraining effect of the crystals on the segment mobility.

EXPERIMENTAL

Data for the molecular structure of the studied samples are presented in *Table 1*. Except where otherwise stated, the studied samples were melt-crystallized during cooling at a rate of 15 K min^{-1} from 443 K in a Schwabenthan compression moulding machine (Polystat 400s).

The dimensions of the samples used in the sorption/desorption experiments were as follows: thickness = 1 mm; width = 10 mm; length = 34.5 mm (except for sample NR, which was 2.5 mm × 35 mm × 35 mm). Before the desorption experiment, the samples were immersed in liquid n-hexane (purity 99%, Merck; density $\rho_l = 656$ kg m^{-3} (298.2 K)) at 298.2 K until sorption equilibrium was attained. Three hours after sorption equilibrium was established, the surface-dried samples were exposed to air at 298.2 K and the desorption experiment was carried out by intermittent weighing of the samples on a Mettler AE balance after different times. The loss of polymer material into the n-hexane liquid during sorption was low (<2 wt% (NR) and <0.6 wt% (PEs)).

The permeability of oxygen was obtained at 298.2 K using a Mocon OX-TRAN 2/20 device. Samples with a thickness of 0.7 mm were mounted in an isolated diffusion cell and were subsequently surrounded by flowing nitrogen gas to remove absorbed oxygen from the samples. The sample had a circular exposure surface area of either 50 cm^2 or 5 cm^2; the latter was achieved by covering a part of the sample with a tight aluminium foil. One side of the sample was initially exposed to flowing air (1% hydrogen, 21% oxygen and 78% nitrogen) at atmospheric pressure while the oxygen concentration was zero on the other side of the specimen. The flow rate (Q) through the specimen was measured during the transient period until the steady-state flow rate (Q_∞) was obtained. The diffusivity D of oxygen (assumed constant) was calculated by fitting the equation [11,12]:

$$\frac{Q}{Q_\infty} = \frac{4l}{(4\pi Dt)^{0.5}} \exp\left(-\frac{l^2}{4Dt}\right) \quad (1)$$

to the $Q(Q_\infty)^{-1}$ vs. t curve using a simplex search algorithm, where l is the thickness of the specimen. Assuming that Henry's law is valid, the solubility S of oxygen is given by:

$$S = \frac{Q_\infty l}{Dp} \quad (2)$$

where p is the partial pressure of oxygen on the high-oxygen-pressure side of the sample.

The lamellar structure was revealed by transmission electron microscopy (TEM) using a JEOL JEM 100 B electron microscope. The TEM studies were carried out on chlorosulfonated samples using the method of Kanig[13] or on samples treated with permanganic acid according to the method developed by Olley and Bassett[14]. Further experimental and analytical details have been presented earlier[15,16]. The average crystal and non-crystalline interlayer thickness values, $\langle L_c \rangle$ and $\langle L_a \rangle$ respectively, were obtained by TEM of chlorosulfonated samples, from which the mass crystallinity could be obtained according to:

$$w_{TEM} = \frac{\langle L_c \rangle}{\langle L_c \rangle + (\rho_L/\rho_{CC})\langle L_a \rangle} \quad (3)$$

where ρ_{CC} and ρ_L are the densities of the crystal-core and

Table 1 Molecular structure of studied polymers

Sample	$\overline{M}_n$ [a]	$\overline{M}_w$ [a]	$\overline{M}_w/\overline{M}_n$	X_{et} [b]
L1	940	1 060	1.1	0
L2	2 200	2 500	1.15	0
L3	10 300	11 600	1.3	0
L4	7 130	10 600	1.5	0
L5	22 400	29 400	1.3	0
L6	12 292	41 700	3.4	0
L7	25 300	110 000	4.3	0
L8	83 400	106 500	1.3	0
L9	14 000	144 000	10.3	0
L10 [c]	19 100	1 040 000	54.45	0
L2/L9	2 200/14 000	2 500/144 000	1.15/10.3	0
B1	8 100	31 300	3.9	1.00
B2	16 900	127 000	7.5	1.50
B3	25 800	128 000	5.0	1.50
B4	34 300	137 000	4.0	0.56
B5	30 900	136 000	4.4	0.19 [e]
B6	9 700	146 000	15.1	0.60 [f]
B7	10 900	170 000	15.6	0.44 [g]
B8	8 700	224 000	25.7	0.50
B9	21 250	258 000	12.1	0.48
NR [c,d]	145 000	664 000	4.6	

[a] By size exclusion chromatography (in g mol^{-1})
[b] Mole per cent of ethyl branches; data by i.r. and ^{13}C n.m.r. spectroscopy
[c] A portion of the sample was insoluble
[d] Uncrosslinked sample
[e] 0.12 mol% of ethyl branches and 0.07 mol% of C_6 or longer branches; by ^{13}C n.m.r. spectroscopy
[f] 0.38 mol% of ethyl branches and 0.22 mol% of C_6 or longer branches; by ^{13}C n.m.r. spectroscopy
[g] Mole per cent of butyl branches; by ^{13}C n.m.r. spectroscopy

liquid-like components: $\rho_{CC} = 1000\,kg\,m^{-3}$ and $\rho_L = 855\,kg\,m^{-3}$ (ref. 17).

The melting endotherms of the samples were obtained in a Perkin-Elmer differential scanning calorimeter (DSC-7) at a heating rate of $10\,K\,min^{-1}$ and the recorded values of heat of fusion (Δh_f) were transformed into mass crystallinity (w_{DSC}) using the total enthalpy method[18], using $293\,kJ\,kg^{-1}$ (ref. 19) as the heat of fusion (Δh_f°) for 100% crystal-core polymer at the equilibrium melting point T_m° (418.5 K)[20]:

$$w_{DSC} = \frac{\Delta h_f}{\Delta h_f^\circ - \int_{T_1}^{418.5}(c_{pa} - c_{pc})dT} \quad (4)$$

where T_1 is an arbitrary temperature below the melting range, and c_{pa} and c_{pc} are the specific heats of the liquid-like and crystal-core components respectively. Data for c_{pa} and c_{pc} reported by Wunderlich and Baur[21] have been used. The Thomson–Gibbs equation[15] was used to calculate the crystal thickness:

$$L_c = \frac{2\sigma T_m^\circ}{(T_m^\circ - T_m)\Delta h_f \rho_{CC}} \quad (5)$$

where L_c is the crystal thickness, σ is the fold surface free energy ($93\,mJ\,m^{-2}$ (ref. 22)), T_m is the melting peak temperature and Δh_f is the heat of fusion ($293\,kJ\,kg^{-1}$).

The superstructure of the samples was assessed by polarized light microscopy on *p*-xylene solution-cast films and small-angle light scattering (SALS) on 200 μm thick samples. From the scattering angle (θ_{max}) corresponding to a maximum in scattered intensity, an average spherulite radius (SR) was obtained according to[23]:

$$SR = \frac{4.09\lambda}{4\pi n_R \sin(\theta_{max}/2)} \quad (6)$$

where $\lambda = 617.6$ nm is the wavelength (He–Ne laser) and $n_R \approx 1.5$ is the average refractive index of the polymer.

The densities (ρ_2) at 296.2 K of the samples were determined in a density gradient column prepared from ethanol and water or isopropanol and diethylene glycol according to ASTM D1505-68, and they were converted to mass crystallinities according to:

$$w_D = \frac{\rho_{CC}(\rho_L - \rho_2)}{\rho_2(\rho_L - \rho_{CC})} \quad (7)$$

Raman spectroscopy was performed at ambient temperature using a Perkin-Elmer near-infra-red FT-Raman 1700X. The number of scans was 1050 (or 258 using a liquid-nitrogen-cooled detector). The runs were interrupted after every 128 scans in order to avoid an extensive temperature rise in the samples.

^{13}C cross-polarized-magic angle spinning n.m.r. spectra (^{13}C CP/MAS n.m.r.) were recorded on a Bruker AMX-300 instrument (at ambient temperature) operating at 75.47 MHz. A double air-bearing probe and zirconium oxide rotor were used. The MAS rate was 5000 Hz. A standard CP pulse sequence was used with a 3.5 μs proton 90° pulse for the L10, L10i and B2 samples and a 4.75 μs proton 90° pulse for the L2 and L6 samples. The contact pulse was 800 μs and the delay between repetitions was 10 s. For each spectrum, 256 transients were recorded, each consisting of 4096 data points, covering a spectral width of 170 ppm for the L2, L6 and L10 samples and 135 ppm for the L10i and B2 samples. Glycine was used for the Hartmann–Hahn matching procedure and as an external standard for the calibration of chemical shifts relative to tetramethylsilane (TMS, $(CH_3)_4Si$). The data point of maximum intensity in the glycine carbonyl line was assigned a chemical shift of 176.03 ppm.

THEORY

Fick's second law of diffusion for a plate geometry was used to model the desorption:

$$\frac{\partial v_1}{\partial t} = \frac{\partial}{\partial x}\left(\frac{D_m}{1 - v_1}\frac{\partial v_1}{\partial x}\right) \quad (8)$$

where D_m is the mutual diffusion coefficient for the actual system with the polymer as the fixed reference frame[8]. It is related to the thermodynamic diffusion coefficient (D_T) through the relationship[3]:

$$\frac{D_m}{1 - v_1} = D_T \frac{\partial \ln a_1}{\partial \ln v_1^a} \quad (9)$$

where a_1 is the activity of the solute in the polymer. The activity correction term can be written[24]:

$$\frac{\partial \ln a_1}{\partial \ln v_1^a} = (1 - v_1^a)(1 - 2\chi v_1^a) \quad (10)$$

where χ is the interaction parameter, which was taken from the work of Castro *et al.*[25] for PE/n-hexane (1.175 at 298.2 K) and from Tewari and Schreiber[26] for NR/n-hexane (0.53 at 298.2 K). The diffusivity in a semicrystalline polymer (D_T) depends on the diffusivity in the non-crystalline component (D_T^a) according to[3]:

$$D_T = (\psi/B)D_T^a \quad (11)$$

where ψ is the detour factor, which takes into account the hindrance to diffusion that originates from the impenetrable crystallites. Peterlin[3] introduced a blocking factor (B), which considers that a portion of the non-crystalline interlayers are too narrow for a penetrant molecule to pass. On the assumption that the volume is invariant during mixing, the fractional free volume outside the crystal core (f^a) is given by[4]:

$$f^a = v_1^a f_1 + v_2^a f_2 \equiv f \quad (12)$$

where v_1^a and v_2^a are solute and polymer volume fractions in the solute–polymer mixture outside the crystal core, and f_1 and f_2 are their respective fractional free volumes. The volume invariance upon mixing was confirmed by volumetric measurements on NR swollen in n-hexane. The thermodynamic diffusivity for a semicrystalline polymer can be written[9]:

$$D_T = \frac{\psi}{B} RTA_d \exp\left(-\frac{B_d}{f_2 + v_1^a(f_1 - f_2)}\right) \quad (13)$$

which may be rearranged as:

$$D_T = D_{T(v_1^a \to 0)} \exp\left(\frac{B_d v_1^a (f_1 - f_2)}{f_2[f_2 + v_1^a(f_1 - f_2)]}\right)$$

$$= D_{T(v_1^a \to 0)} D^*_{T(v_1^a)} \quad (14)$$

where

$$D_{T(v_1^a \to 0)} = \frac{\psi}{B} RTA_d \exp\left(-\frac{B_d}{f_2}\right) \quad (15)$$

A_d and B_d are functions of the size and shape of the penetrant molecules and they are reported to be independent of temperature[5]. B_d may be related to the minimum hole size required for a diffusional jump of the whole or a part of the penetrant molecule[4]. The B_d parameter for n-hexane was taken to be 0.8[4]. The pre-exponential factors may be brought together in a single parameter A according to:

$$A = (\psi/B)RTA_d \quad (16)$$

In the fitting of equation (13) to the experimental desorption data, the A and f_2 parameters were adjustable. The fractional free volume of n-hexane at 298.2 K was set to 0.168 using data of Fleischer[8].

The concentration profiles during the desorption measurement were generated by an implicit multistep backward differentiation formula[9,27]. The right-hand side of equation (8) is given in the Appendix. The mean penetrant concentration in the specimen as a function of time was obtained through numerical integration of the concentration profiles using Simpson's method combined with the Romberg routine to obtain higher accuracy. The optimization was carried out by minimizing the sum of the squares of the differences between the experimental and the predicted desorption data.

RESULTS AND DISCUSSION

Raman spectroscopy can be used to assess the contents of crystal core (CC), liquid-like (L) and interfacial (I_{CC} and I_L) components using data from the CH_2 rocking (700–970 cm^{-1}), C–C stretching (1020–1160 cm^{-1}), CH_2 twisting (1250–1350 cm^{-1}) and CH_2 bending (1390–1510 cm^{-1}) regions[10,28–34]. To illustrate changes in the Raman spectrum with changing crystallinity, the spectra of hexacontane, L10 and n-octadecane are shown in *Figure 1*. The spectra of n-octadecane (fully liquid-like) and hexacontane (fully crystalline) and of the low-molar-mass linear PEs L1 and L2 were useful in making phase assignments of the different Raman peaks in the CH_2 twisting region: 1295 cm^{-1} is due to CC and I_{CC}, and 1303 cm^{-1} originates from L and I_L. The latter is in accordance with data of Strobl and Hagedorn[28] and of Mutter *et al.*[10]. The low-frequency tail centred at 1270 cm^{-1} was present in all the samples.

The C–C stretching region (1020–1160 cm^{-1}) may provide the same information as is given in the CH_2 twisting region[28]. However, owing to its complexity, it is not analysed here[35,36].

The assignments of the peaks of the CH_2 bending region were as follows (*Figure 1*): 1417 cm^{-1} is due to CC (both orthorhombic and monoclinic crystal forms[28,37]), the narrow 1440 and 1462 cm^{-1} peaks are due to CC and possibly also parts of the interphase (absent in the liquid n-octadecane spectrum), and the broad and asymmetric peak centred at 1140 cm^{-1} originates from L (and possibly parts from I_L).

The following equations based on the Lorentz equation were fitted to the intensity (I) vs. wavenumber (ν) data in the CH_2 twisting region:

$$I_{(1250-1350)} = \sum_k \frac{I_k^p}{\{1 + [(2/a_k)(\nu - \nu_k)]^2\}^q}$$

$$k = 1270, 1295, 1303\ cm^{-1} \quad (17)$$

where I_k^p is the intensity at the kth peak, a_k is the peak width at half the peak height ($I_k^p/2$), and ν_k is the wavenumber corresponding to the kth peak. The exponent q was set to 2 for all peaks. A similar equation was fitted to the intensity profile in the CH_2 bending

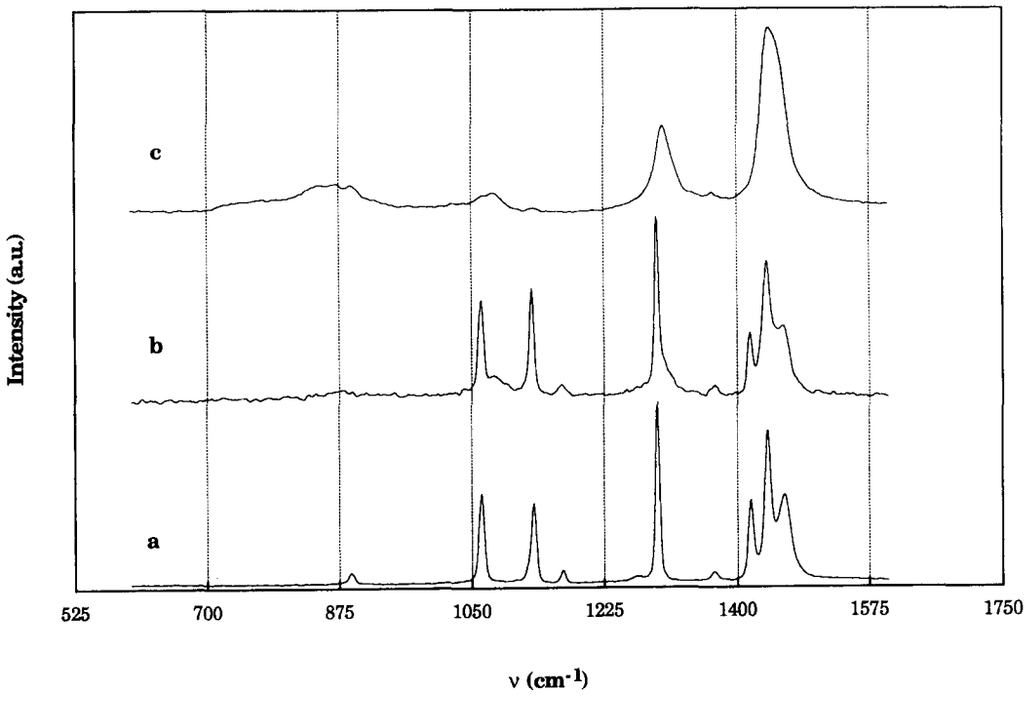

Figure 1 Raman spectra of (a) hexacontane, (b) L10 and (c) n-octadecane

region (1390–1510 cm^{-1}) and it included the following peaks: $k = 1417$, 1440 and 1462 cm^{-1}; $q = 2$. The integration of the intensities associated with each of the peaks was performed according to a quadrature procedure with a relative error smaller than 0.003.

According to Mutter *et al.*[10], the CH_2 rocking mode is the mode that is most sensitive to the conformational state of the polymer chain, and its broad intensity halo (700–970 cm^{-1}) with a maximum around 870 cm^{-1} (absent in hexacontane, L1 and L2) has therefore here, in accordance with Mutter *et al.*[10], been assumed to correspond to the truly liquid-like component (L) of the polymer. With $I_{(1250-1350)}$ as an internal standard[28], the liquid-like content (ω_L) was obtained using the spectrum of n-octadecane as a standard for a fully liquid-like component ($w_L = 1$):

$$w_L = \frac{I_{(700-970)}}{I_{(1250-1350)}} \times \left(\frac{I_{(700-970)}}{I_{(1250-1350)}} \right)^{-1}_{(w_L=1)} \quad (18)$$

The intensities in equation (18) were obtained by numerical integration of the peaks in the spectra. The in-plane CH_3 rocking peak at 890 cm^{-1} was subtracted from the CH_2 rocking halo of the n-octadecane sample.

The total content of the liquid-like and the interfacial liquid-like components ($w_L + w_{I_L}$) was obtained according to:

$$w_L + w_{I_L} = \frac{I_{1303}}{I_{(1250-1350)}} \quad (19)$$

The value w_{I_L} was then calculated from equations (18) and (19). The crystal-core content (w_{CC}) was obtained principally in accordance with the method of Strobl and Hagedorn[28], in this particular case using the spectrum of hexacontane as a standard for fully crystalline material ($w_{CC} = 1$):

$$w_{CC} = \frac{I_{1417}}{I_{(1250-1350)}} \times \left(\frac{I_{1417}}{I_{(1250-1350)}} \right)^{-1}_{(w_{CC}=1)} \quad (20)$$

The mass fraction of the crystal-like interphase ($w_{I_{CC}}$)

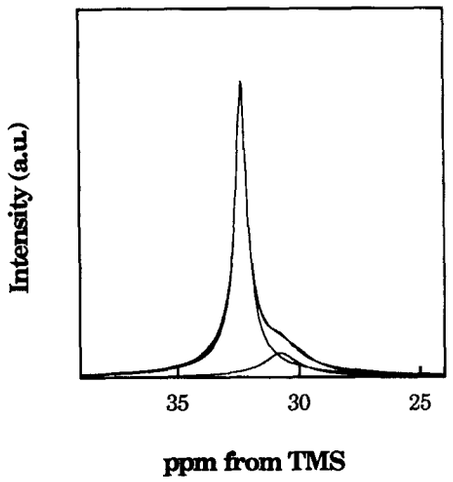

Figure 2 ^{13}C CP/MAS n.m.r. spectrum of L6. Two Lorentz peaks centred at 30.7 and 32.3 ppm are fitted to the spectrum

Table 2 Crystallinities of studied polymers[a]

Sample	w_{DSC} (±0.025)	w_D (±0.025	w_{TEM} (±0.05)	w_{CC} (±0.025)	$w_{I_{CC}}$ (±0.025)	w_{I_L} (±0.025)	w_L (±0.025)	w_{NMR} (±0.025)
L1	0.956	–	–	0.967	0.033	0.000	0.000	–
L2	0.948	–	–	0.940	0.060	0.000	0.000	1.000
L3	0.864	0.836	–	0.769	0.145	0.000	0.086	–
L4	0.820	0.850	–	0.750	0.120	0.057	0.073	–
L5	0.755	0.769	0.751	0.703	0.099	0.082	0.116	–
L6	0.765	0.770	0.706	0.723	0.110	0.044	0.1213	0.820
L7	0.749	0.763	0.718	0.704	0.124	0.081	0.091	–
L8	0.649	0.672	0.626	0.570	0.121	0.105	0.204	–
L9	0.758	0.767	–	0.722	0.100	0.043	0.135	–
L10	0.517	0.552	0.604	0.457	0.143	0.216	0.184	0.643
L10i[b]	0.697	–	–	0.627	0.120	0.087	0.166	0.704
L2/L9	0.928	–	–	0.905	0.072	0.004	0.019	–
B1	0.558	0.630	–	0.475	0.198	0.110	0.217	–
B2	0.447	0.498	–	0.352	0.210	0.100	0.338	0.612
B3	0.432	0.486	0.510	0.367	0.180	0.105	0.348	–
B4	0.558	0.601	0.569	0.478	0.186	0.109	0.227	–
B5	0.662	0.670	0.642	0.591	0.174	0.078	0.157	–
B6	0.625	0.657	0.675	0.573	0.150	0.095	0.182	–
B7	0.620	0.654	0.662	0.553	0.137	0.084	0.226	–
B8	0.573	0.619	–	0.530	0.168	0.099	0.203	–
B9	0.585	0.618	0.622	0.504	0.163	0.098	0.235	–

[a] From d.s.c. (w_{DSC}), from density measurements (w_D), from TEM (w_{TEM}), from Raman spectroscopy (w_{CC}, $w_{I_{CC}}$, w_{I_L} and w_L and from ^{13}C CP/MAS n.m.r. spectroscopy (w_{NMR})
[b] Crystallized at 402 K for 30 days

is then given by:

$$w_{I_{CC}} = 1 - w_L - w_{I_L} - w_{CC} \quad (21)$$

Figure 2 shows a ^{13}C CP/MAS n.m.r. spectrum of a linear PE of medium molar mass. The spectrum consisted of a narrow component peaking at 32.3 ppm associated with orthorhombic CC and most probably of I_{CC}, and a broader peak at 30.7 ppm due to L (and perhaps I_L). A third peak at 33.7 ppm, originating from the monoclinic crystal form, appeared in some of the samples (L2, L10 and L10i). The composite spectrum was resolved into Lorentzian components (the exponent q ranged between 0.7 and 1) principally equivalent to equation (17). The resolved peaks were integrated using the quadrature method, yielding $I_{30.7}$, $I_{32.3}$ and $I_{33.7}$. The mass crystallinity (w_{NMR}) was obtained according to:

$$w_{NMR} = \frac{I_{32.3} + I_{33.7}}{I_{30.7} + I_{32.3} + I_{33.7}} \quad (22)$$

Table 2 presents the data for the mass crystallinity and mass fractions of L, I_L, I_{CC} and CC components. There is a fair agreement in the crystallinity obtained by density, d.s.c. and TEM (*Table 2*): w_D is on average 0.013 larger than w_{DSC} for linear PE, whereas for branched PE the mean difference is 0.041; w_D is on average 0.024 larger than w_{TEM} for linear PE, and for the branched polymers there is a perfect match between the two averages. The densities of the lowest-molar-mass samples, L1, L2 and L2/L9, were anomalously low in view of their high crystallinity values, and a comparison between crystallinity data obtained by d.s.c. and density measurements indicated that these samples contained approximately 1% of pores.

The crystallinity from density/d.s.c./TEM data was always intermediate between w_{CC} and $w_{CC} + w_{I_{CC}}$ (*Table 2*). The mean difference between $(w_{CC} + w_{I_{CC}})$ and w_D was 0.055 (average value) and was practically independent of mass crystallinity. The average difference between w_D and w_{CC} was 0.089; this quantity decreased strongly increasing mass crystallinity. The density of I ($I_{CC} + I_L$) was calculated to be $907.1 \pm 20\,kg\,m^{-3}$ for the studied samples (L1, L2 and L2/L9 excluded) using the equation:

$$\rho_I = \frac{w_I}{1/\rho_2 - w_{CC}/\rho_{CC} - w_L/\rho_L} \quad (23)$$

Strobl and Hagedorn[28] suggested that the I_{CC} component has a density close to the extrapolated value of the pure melt, whereas Mandelkern *et al.*[29] reported a density of I_{CC} closer to that of the crystal-core component. Cheng *et al.*[38] suggested, on the basis of n.m.r. data, that the interphase has a density similar to that of the crystal core. It has been suggested that I_{CC} consists of chain segments mostly in the *trans* conformation but without the lateral order characteristic of the crystal core[28,29,38]. Kitamaru *et al.*[39] revealed by n.m.r. the presence of a component with a *trans* content intermediate between that of the crystal core and the liquid-like components, most probably to be identified with both I_{CC} and I_L components. It is generally believed that the interfacial components are spatially located between the CC and L components[10,28,38,39]. Sample L2 with 6% of I_{CC} according to Raman spectroscopy showed no signs of *gauche* isomers according to n.m.r.

The crystallinities obtained from n.m.r. data were on average 0.065 larger than the density crystallinities but were very similar indeed to $w_{CC} + w_{I_{CC}}$ (*Table 2*, column 5 + column 6).

A comparison of the high-crystallinity sample crystallized at $15\,K\,min^{-1}$ (L10) and isothermally crystallized (L10i) shows that the amount of liquid-like component (w_L) is approximately the same in both samples. Slow crystallization led to a decrease in I_L content and to an increase in CC content whereas the I_{CC} content was the same for both samples. The non-crystalline component (i.e. non-crystal-core material) of the L10 sample contained only 33% of the liquid-like component (compared to 52% for B2).

Figures 3 and *4* show expected trends for crystallinity as a function of molar mass and degree of chain branching, respectively. The decrease in mass crystallinity with increasing molar mass for linear PE is in accordance with earlier data of Tränkner *et al.*[15]. The

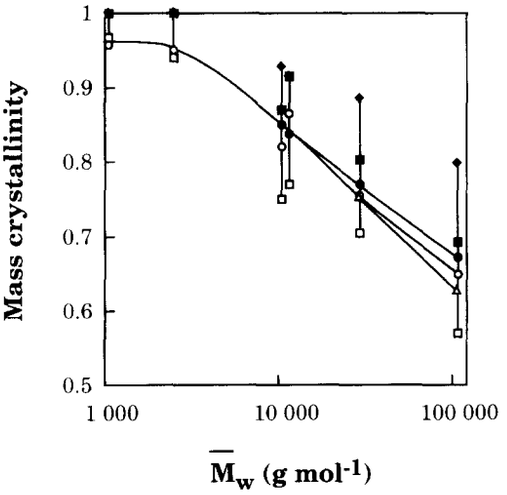

Figure 3 Mass crystallinity as a function of molar mass for linear PE fractions. Crystallinities were obtained by d.s.c. (○), density measurements (●), TEM (△) and Raman spectroscopy (□, w_{CC}; ■, $w_{CC} + w_{I_{CC}}$; ◆, $w_{CC} + w_{I_{CC}} + w_{I_L}$)

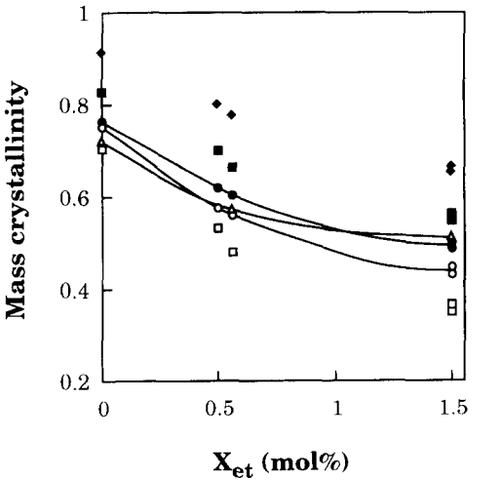

Figure 4 Mass crystallinity as a function of mole per cent of ethyl branches for PEs of similar molar masses. Crystallinities were obtained by d.s.c. (○), density measurements (●), TEM (△) and Raman spectroscopy (□, w_{CC}; ■, $w_{CC} + w_{I_{CC}}$; ◆, $w_{CC} + w_{I_{CC}} + w_{I_L}$)

crystallinity range for the linear PEs is 0.6–1.0. *Figure 4* shows that the mass crystallinity decreases in a non-linear manner with increasing degree of chain branching. The decrease in crystallinity is approximately 0.25 per mole per cent of ethyl groups, which is consonant with earlier reported data[15]. In conclusion, PEs with a very sizeable variation in L and I ($I_{CC} + I_L$) contents, 0–35% and 3–36% respectively, were prepared for the diffusivity measurements. Several methods were used for the assessment of CC, I and L components, and the data obtained were internally consistent.

A selection of transmission electron micrographs showing the main morphological trends are presented in *Figure 5*. *Figure 5a* shows a typical lamellar structure of a linear PE of intermediate molar mass containing roof or straight lamellae arranged mostly in large lamellar stacks. With increasing molar mass, both the number of lamellae in the lamellar stacks and the average lamella width decrease (*Figures 5b* and *5c*). In branched PEs of intermediate or high molar mass (*Figure 5d*), the lamellae are relatively short, thin and curved.

The majority of the samples were crystallized at a constant cooling rate (15 K min^{-1}) from the melt. The average thicknesses of crystals (L_c) and non-crystalline interlayers (L_a) were obtained from melting-point and crystallinity data by d.s.c. The results of all morphological assessments are summarized in *Table 3*.

Both the average crystal (L_c) and average non-crystalline interlayer (L_a) thicknesses increased with increasing molar mass for the linear PEs (*Figure 6*). The substantial increase in L_a from close to zero to 15 nm is particularly important for the transport properties. The long period ($L_c + L_a$) of the linear PEs increased with increasing molar mass from 8 nm at $\overline{M}_w = 1000$ g mol^{-1} by 12 nm per order of magnitude in molar mass up to $\overline{M}_w = 1\,000\,000$ g mol^{-1} (*Figure 7*). The width of the crystal lamellae decreased strongly with increasing molar mass; there is a linear decreasing trend in a linear w_i vs log $\overline{M}_w$ diagram from 1.2 μm for $\overline{M}_w = 30\,000$ g mol^{-1} to 0.3 μm for $\overline{M}$ w = 1 000 000 g mol^{-1} (*Table 3*).

The branched PEs exhibited, as expected, a decrease in L_c and an increase in L_a with increasing degree of branching (*Table 3*). The long period remained, however, approximately the same (28 ± 2.5 nm) for all branched PEs. The variations in molar mass between the studied branched PEs were relatively small (*Table 1*) and there is only a small difference between the long-period data for linear and branched PEs of the same molar mass (*Figure 7*). There is a tendency for the lamellar width to decrease with increasing degree of branching (cf. *Tables 1* and *3*).

Most of the samples exhibited banded spherulites except for the PEs with the lowest molar masses, which exhibited non-banded spherulites or even axialites (*Table 3*). The linear PEs contained spherulites of radii between 4 and 11 μm, whereas the branched polymers exhibited spherulites of radii typically between 2 and 3 μm.

Data for the equilibrium solubilities of n-hexane and oxygen in PE and NR are presented in *Table 4*. *Figure 8* presents data for the equilibrium penetrant (n-hexane and oxygen) solubility in the non-crystalline fraction as a

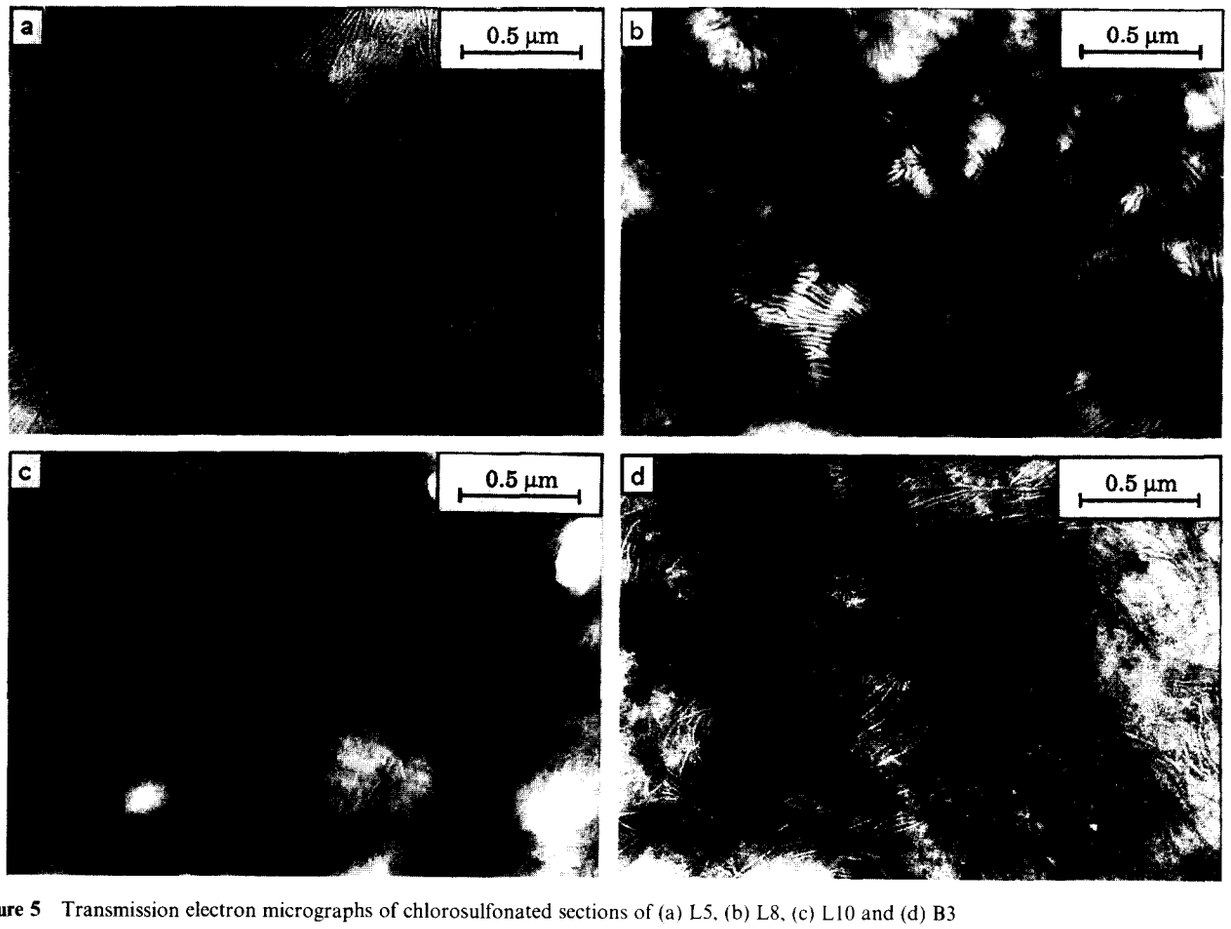

Figure 5 Transmission electron micrographs of chlorosulfonated sections of (a) L5, (b) L8, (c) L10 and (d) B3

Table 3 Morphology of studied polymers

Sample	*SS*[a]	*SR*[b]	L_c[c] (±0.5)	L_a[d]	$L_{a,min}$[e]	w_l[f]
L1	–	–	7.2	0.4	–	
L2	A	6.9[g]	12.1	0.8	–	>1300[h]
L3	NBS/A	10.8[g]	18.5	3.4	–	–
L4	NBS/A	8.8[g]	18.5	4.8	–	–
L5	BS	8.9	20.2	7.7	3.5	1203
L6	BS	7.9	19.4	7.0	5.6	914
L7	BS	4.0	21.6	8.4	3.1	727
L8	BS	3.7	22.0	13.9	7.7	809
L9	BS	3.9	23.1	8.6	–	739[f]
L10	RL	–	21.8	23.8	10.5	386
L10i	–	–	42.75	21.7	–	–
L2/L9	NBS/A	3.8[g]	15.4 (11.5)	1.4 (1.0)	–	1188[f]
B1	BS/NBS/A	5.6	10.1	9.4	–	397
B2	BS	2.95	11.9	17.3	–	358[i]
B3	BS	3.4	11.7	18.0	7.5	396
B4	BS	2.5	14.4	13.4	8.3	476
B5	BS	2.4	19.0	11.4	6.0	750
B6	BS	2.1	16.6	11.7	3.3	516
B7	BS	2.4	16.6	11.9	6.6	391
B8	BS	1.9	13.8	12.0	–	506
B9	BS	3.7	14.1	11.7	4.4	255

[a] Superstructure (*SS*) as assessed by polarized light microscopy: BS, banded spherulites; NBS, non-banded spherulites; A, axialites, RL, random lamellar structure
[b] Average spherulite (axialite) radius (in μm), by s.a.l.s.
[c] Crystal thickness (in nm), calculated from melting-point data (d.s.c.)
[d] Average thickness of non-crystalline interlayers (in nm), calculated from crystal thickness and crystallinity data
[e] Minimum thickness of non-crystalline interlayers (in nm), by TEM
[f] Lamellar width (in nm) measured by TEM of chlorosulfonated samples
[g] By polarized light microscopy
[h] Value derived from L9 and L2/L9
[i] Lamellar width (in nm) as obtained by TEM of samples etched with permanganic acid

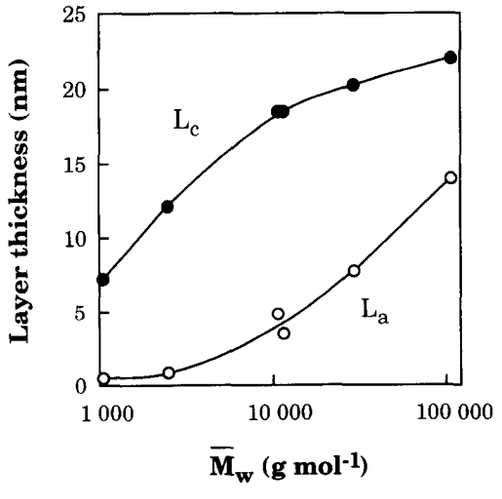

Figure 6 Crystal (L_c (○)) and non-crystalline interlayer (L_a (●)) thicknesses of linear PE fractions as a function of molar mass; L_c and L_a were calculated from d.s.c. data considering both the Thomson–Gibbs equation and the d.s.c. crystallinity

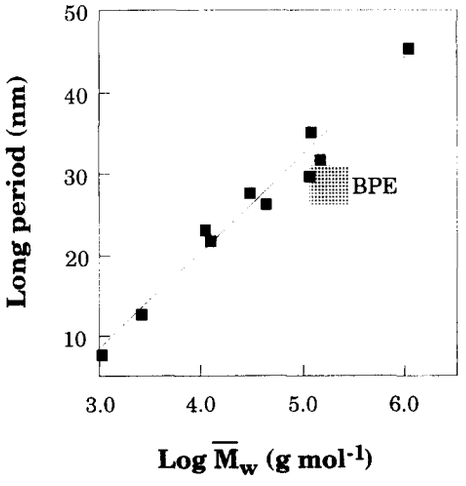

Figure 7 Long periods ($L_c + L_a$) of linear PE and branched PE (BPE) as a function of molar mass, calculated from d.s.c. data considering both the Thomson–Gibbs equation and the d.s.c. crystallinity

Table 4 Solubilities and diffusivities of studied polymers at 298.2 K

Sample	w_1[a]	S[b]	$D_{T(v_1^a \to 0)}$[c]	D[d]
L1	–	–	–	–
L2	0.0135	–	8.40×10^{-10}	–
L3	0.039	–	–	–
L4	0.038	–	–	–
L5	0.040	–	–	–
L6	0.041	0.020	1.43×10^{-9}	1.42×10^{-7}
L7	0.043	–	1.43×10^{-9}	–
L8	0.051	–	2.62×10^{-9}	–
L9	0.043	0.023	2.43×10^{-9}	1.49×10^{-7}
L10	0.060	0.033	7.97×10^{-9}	4.08×10^{-7}
L2/L9	0.025	–	1.39×10^{-10}	–
B1	0.066	–	–	–
B2	0.106	0.060	1.40×10^{-8}	4.50×10^{-7}
B3	0.106	–	1.32×10^{-8}	–
B4	0.060	–	3.01×10^{-9}	–
B5	0.050	–	1.30×10^{-9}	–
B6	0.051	–	4.17×10^{-9}	–
B7	0.055	0.027	7.10×10^{-9}	2.64×10^{-7}
B8	0.056	0.028	2.47×10^{-9}	2.01×10^{-7}
B9	0.055	–	–	–
NR	0.571[e]	0.174	3.24×10^{-7}[e,f]	1.46×10^{-6}

[a] Mass fractions of dissolved n-hexane
[b] Solubility of oxygen (cm^3(STP) cm^{-3} atm^{-1})
[c] Zero-concentration diffusivity of n-hexane (cm^2 s^{-1})
[d] Diffusivity of oxygen (cm^2 s^{-1})
[e] Crosslinked sample; $\overline{M}_c = 2900$ g mol^{-1}
[f] Average value from calculations using dry and swollen sample thicknesses

function of crystallinity. The mass fractions of the three components (CC, I ($I_{CC} + I_L$ are brought together) and L) shown in *Table 2* were converted into volume fractions according to:

$$v_i = \frac{w_i \rho_2}{\rho_i} \quad i = \text{CC, I or L} \tag{24}$$

The volume fraction of solute was calculated as:

$$v_1 = \frac{1}{1 + \rho_1(1 - w_1)/\rho_2 w_1} \tag{25}$$

where w_1 is the mass fraction of solute.

The lowest-molar-mass sample, L1, fragmented during its exposure to n-hexane, most probably due to the lack of tie chains in this sample. Raman spectroscopy showed that the fragmented sample contained crystal-core material.

Two of the samples (three with L1) contained pores, and the modelling of the sorption kinetics shown later in *Figure 10* indicated that 70–80% of the penetrant was included in the polymer component, the rest being included in microvoids. The equilibrium penetrant solubility data of these samples presented in *Figure 8* were accordingly corrected without considering the fraction of penetrant filling microvoids.

One important feature shown in *Figure 8* is the increase in equilibrium penetrant solubility in the non-crystalline components with increasing crystallinity in the high-crystallinity range. The samples included in this crystallinity range were all linear PEs of different molar masses, the samples with the lowest molar masses showing the largest non-crystalline equilibrium penetrant solubility. In accordance with reported dilatometric data[4,40], it can be proposed that the chain ends bring extra free volume into the non-crystalline components.

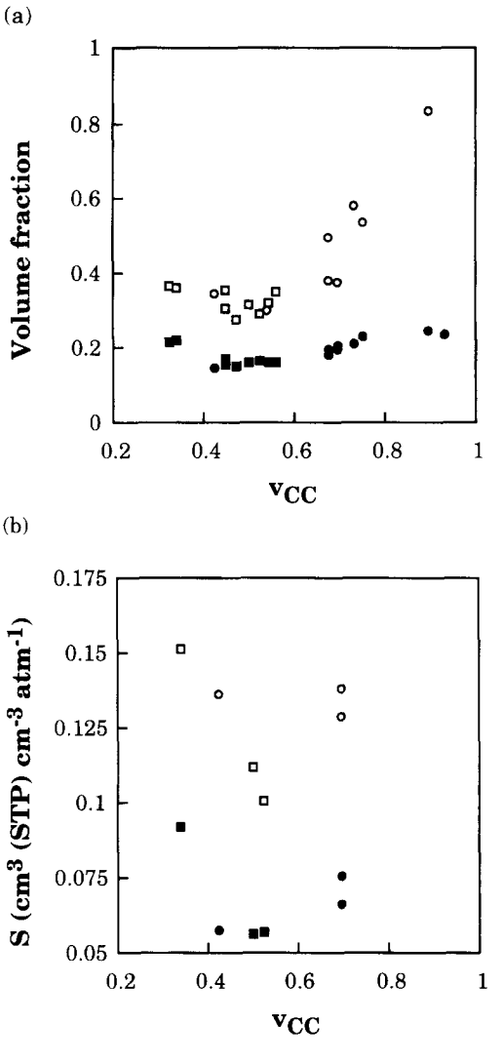

Figure 8 Specific solubility of (a) n-hexane and (b) oxygen in the L component (○, linear PE; □, branched PE) or in the L + I (I = $I_{CC} + I_L$) component (●, linear PE; ■, branched PE) as a function of crystal-core content

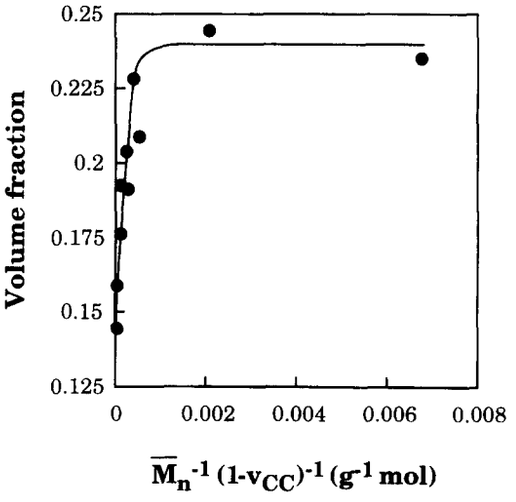

Figure 9 Specific solubility in the L + I component for linear PE as a function of the content of chain ends in the non-crystalline component

A simple assumption that can be made is that each chain end contributes with a certain extra free volume, implying that the equilibrium penetrant solubility should be proportional to the concentration of chain ends in the non-crystalline fractions. This hypothesis is critically tested in *Figure 9* and its failure is clearly shown.

There is definitely an increase in equilibrium solubility with increasing concentrations of chain ends but the increase is markedly non-linear. The penetrant solubility in the lowest-molar-mass samples is much less than that predicted from an extrapolation of the high-molar-mass data. It may be suggested that the increasing free volume originating from chain ends in the low-molar-mass PEs is partly counteracted by the constraining effect of the crystals, since these samples also showed the highest degree of crystallinity.

Figures 8a and *8b* also show that the penetrant solubility increases in the two samples of lowest crystallinity, which are the two samples with the highest degree of chain branching (1.5 mol% of ethyl branches). The increase in solubility can be attributed to the high concentration of ethyl groups, which is expected to increase the free volume of the non-crystalline components.

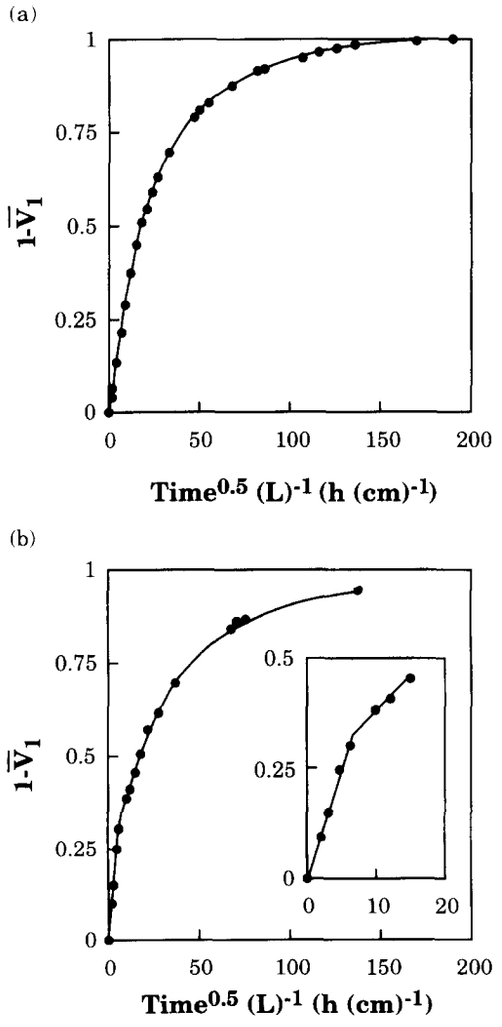

Figure 10 Normalized n-hexane desorption curves (●) for (a) L8 and (b) L2. The line indicates the best fit of the model (equation (13) and Appendix in (a), and equations (13) and (26) and Appendix in (b)). The inset demonstrates the 'knee' in the desorption curve

Figure 10 presents experimental and theoretical (fitted) desorption curves for L2 and L8. L8 exhibited a 'smooth', simple type of desorption curve, which was typical of the majority of the samples studied. The equations presented in the theoretical section and in the Appendix could be fitted to the experimental data. The desorption curve of L2 exhibited a pronounced break at $1 - v_1 \approx 0.3$ indicating the simultaneous occurrence of pore diffusion (convection) and conventional diffusion. Sample L2/L9 exhibited a similar break in the desorption curve. On the assumption that the pores formed a continuous network in the polymer and that the proportion of solute in the pores decreased

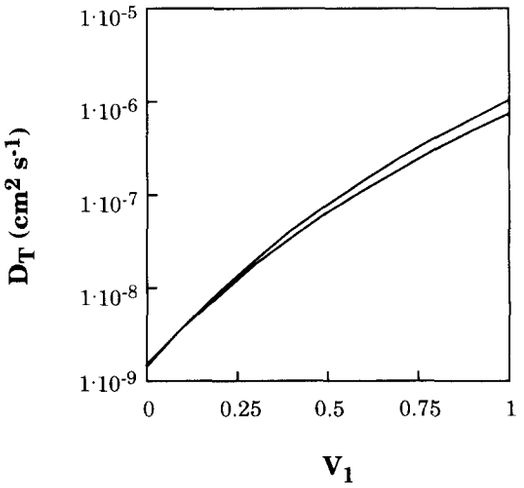

Figure 11 Thermodynamic diffusivity (D_T) as a function of normalized penetrant concentration (V_1) for L6 (lower curve) and L7 (upper curve). The normalization refers to the penetrant saturation concentration for each sample

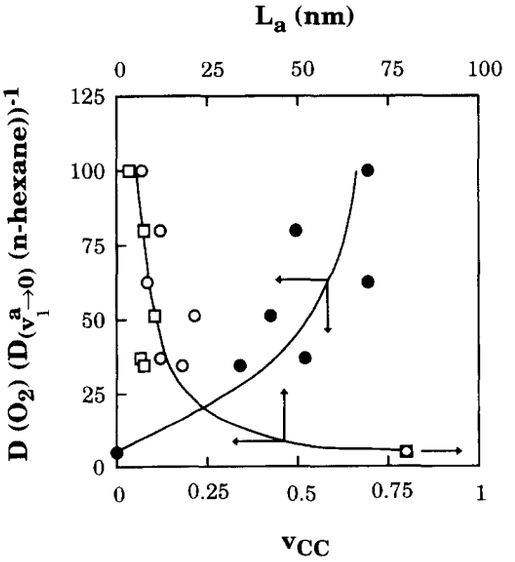

Figure 12 The ratio of oxygen diffusivity (equation (1)) and zero-concentration n-hexane diffusivity (equation (15)) as a function of volume crystallinity (v_{CC}) (●) and minimum non-crystalline interlayer ($L_{a,min}$ (TEM)) (□) and d.s.c.-assessed non-crystalline interlayer thickness (L_a) (○)

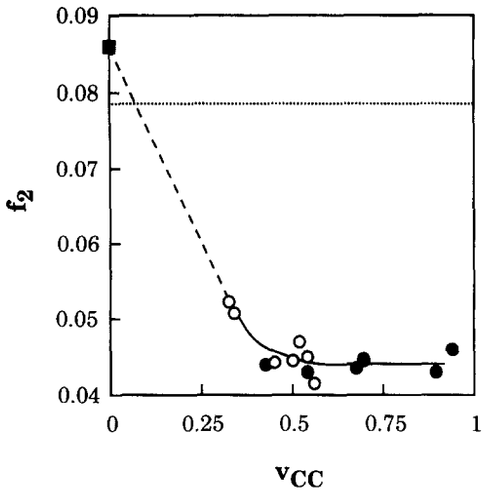

Figure 13 Fractional free volume (f_2) obtained from n-hexane desorption data as a function of volume crystallinity; (●) linear PE, (○) branched PE and (■) NR. Dotted line represents the liquid-like f_2 value obtained from equation (33) for linear PE

exponentially with time, the following expression was derived:

$$\frac{\partial v_1^T}{\partial t} = \frac{\partial v_1}{\partial t} + \frac{\partial v_1^p}{\partial t} = \frac{\partial}{\partial x}\left(\frac{D_m}{1-v_1}\frac{\partial v_1}{\partial x}\right) - K_p(v_1^T - v_1) \quad (26)$$

where v_1^T, v_1^p and K_p are the total solute volume fraction, the solute pore volume fraction and a pore solute-loss rate constant. The fitting of equation (26) to experimental desorption data revealed that the initial proportion of solute in the pores was 0.2 (L2) and 0.3 (L2/L9) with reference to that totally sorbed in the sample. The value of K_p ranged from 0.0005 (L2/L9) to 0.004 (L2) depending on sample thickness.

In *Table 4*, the zero-concentration diffusivities ($D_{T(v_1^a \to 0)}$) of n-hexane in PE and NR calculated with equation (14) are tabulated together with oxygen diffusivities, and in *Figure 11*, D_T vs. V_1 curves are presented for L6 and L7 showing the effects of different f_2 values on the concentration dependence of the diffusivity ($f_2(L6) > f_2(L7), D_{T(v_1^a \to 0)}(L6) = D_{T(v_1^a \to 0)}(L7)$).

In *Figure 12*, the relative diffusivities of oxygen and n-hexane are plotted against volume crystallinity and against the average and minimum non-crystalline interlayer thicknesses. The ratio of oxygen to n-hexane diffusivity increases with increasing crystallinity and with decreasing average amorphous layer thickness. The data indicate that the constraining effect of the crystals more severely retards the diffusivity of larger molecules than of smaller molecules. Blocking effects (influence the *B* factor) are believed to be small for these samples since non-crystalline interlayers (L_a) as thin as 0.8 nm readily permit n-hexane diffusion (see diffusivity data on L2, *Table 4*). The average fractional free volumes (f_2) of the interfacial and liquid components were calculated from the diffusivity data. The results are shown in *Figure 13*. The non-crystalline free volume decreased markedly with increasing crystallinity in the low-crystallinity range, whereas for the linear PEs with crystallinities between 60 and 90% it remained practically constant. It should be noted that there is a dramatic increase in the concentration of chain ends in the non-crystalline phase with increasing crystallinity in this crystallinity range (*Tables 1* and *2*). The data presented in *Figure 13* indicate that the constraining effect of the crystals is compensated for by the plasticizing effect of the chain ends, which results in the approximately constant f_2 value in this crystallinity region. A more general statement that the data of *Figure 13* most clearly demonstrate is that the 'old' two-component model for PE is inadequate. There is thus a need to include more than two components in the analysis of diffusivity data.

In the following treatment of the diffusivity data, the interphase (I) is considered as the sum of the I_{CC} and I_L components. The fractional free volume of the non-crystalline part of the polymer was divided into two components:

$$f_2 = v_2^I f_2^I + v_2^L f_2^L \quad (27)$$

such that

$$v_2^I + v_2^L = 1 \quad (28)$$

where v_2^I and v_2^L are the volume fractions of the interphase and liquid-like polymer and f_2^I and f_2^L are their fractional free volumes. It is assumed that the volume of the non-crystalline system is a simple, additive function based on the volumes of the pure components. The fractional free volumes can in this case be expressed as:

$$f^I = (v_2^I)^\circ f_2^I + [1 - (v_2^I)^\circ] f_1 \quad (29)$$

$$f^L = (v_2^L)^\circ f_2^L + [1 - (v_2^L)^\circ] f_1 \quad (30)$$

where $(v_2^I)^\circ$ and $(v_2^L)^\circ$ are the volume fractions of the interphase and liquid-like component in the mixture with the solvent. Combination of equations (27)–(30) yields the following expressions:

$$f = f_2^L + v_2^I(f_2^I - f_2^L) + v_1^a[f_1 - f_2^L + (v_1^I)^\circ(f_2^L - f_2^I)] \quad (31)$$

$$(v_1^I)^\circ + (v_1^L)^\circ = 1 \quad (32)$$

where $(v_1^I)^\circ$ and $(v_1^L)^\circ$ are the equilibrium volume fractional distributions of solute between the interphase and liquid-like components respectively. In the absence of a diffusional liquid-like fractional free volume for PE, dilatometric and viscosity data were used. The fractional free volume of the liquid-like component is given by:

$$f_2^L = f_{2g}^L + \Delta\alpha(T - T_g) \quad (33)$$

where $f_{2g}^L = 0.025$ (ref. 41) is the fractional free volume at the glass transition temperature ($T_g = 203.2$ K according to Boyd[42]), and $\Delta\alpha$ is the difference between the thermal expansivity of the liquid and glassy states. The following values were used for the liquid and glassy thermal expansivities: $8.8 \times 10^{-4}\ m^3\ kg^{-1}\ K^{-1}$ (linear polyethylene)[43] and $2 \times 10^{-4}\ m^3\ kg^{-1}\ K^{-1}$ (ref. 44). Prior to insertion of these values in equation (33), they were divided by the specific volume of the liquid-like component (at 298.2 K). In order to use the calculated thermal expansivity values, f_{2g}^L must be multiplied by the ratio of specific volume of the liquid at the glass transition[43] and at 298.2 K. An f_2^L value was calculated to be 0.0784 for linear PE and it was used for all samples in the calculations. A maximum difference in thermal

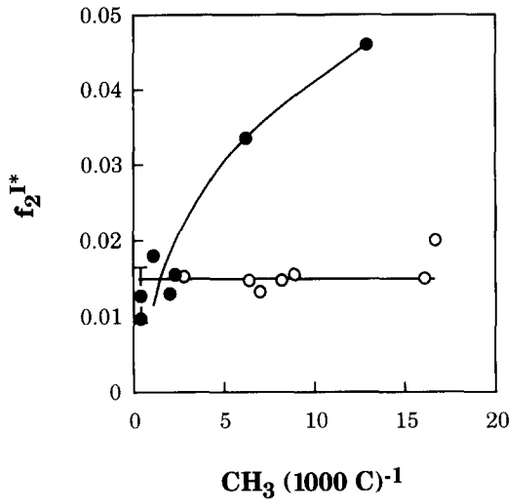

Figure 14 Corrected interphase fractional free volume f_2^{I*} as a function of methyl content for linear PE (●) and branched PE (○). Upper and lower values of error bars (L10) indicate the cases of no interphase swelling ($(v_1^I)^\circ = 0$) and homogeneous swelling ($(v_1^I)^\circ = v_2^I$)

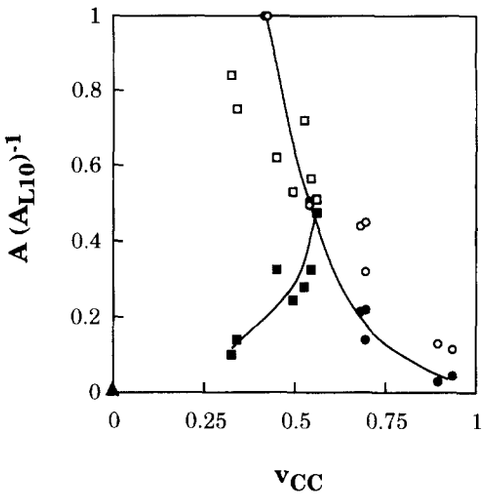

Figure 15 L10-normalized A factors calculated from n-hexane desorption data as a function of v_{CC}: (●) linear PE, (■) branched PE, (▲) NR. Equation (35) is indicated by (○) for linear PE and (□) for branched PE

expansivity between linear and branched liquid PE amounting to 13% was calculated from data of Zoller[45].

Calculated f_2^I values ranged between 0.017 and 0.035 for most samples. In *Figure 14*, a corrected interphase fractional free volume:

$$f_2^{I*} = f_2^I\left(\frac{w_{I_{CC}}}{w_{I_{CC}} + w_{I_L}}\right) \tag{34}$$

is presented as a function of methyl group contents for both linear and branched PE. The calculations were made for $(v_1^I)^\circ = v_2^I$ and $(v_1^I)^\circ = 0$, i.e. for homogeneous swelling and for no interphase swelling respectively. Both cases yielded approximately the same f_2^{I*} values (except for L10, where the upper and lower values in *Figure 14* are for $(v_1^I)^\circ = 0$ and $(v_1^I)^\circ = v_2^I$ respectively). In the case of $(v_1^I)^\circ = 0$, v_1^a is the penetrant concentration based on the polymer liquid-like content. The fact that the scattering in f_2^I data decreases with the use of the correction indicates that the I_{CC} component has a lower fractional free volume than the I_L component. As can be seen in *Figure 14*, the use of a single liquid-like fractional free volume results in an approximately constant f_2^{I*} for samples with intermediate methyl contents; in this region f_2^L, $f_2^{I_L}$ and $f_2^{I_{CC}}$ may be considered constant. For these materials, the fractional free volume of the total polymer is determined by the amount of each of the three non-crystalline components. Small deviations occur from this simple scheme for samples of very high molar mass or a high degree of branching. The strong deviation of the low-molar-mass linear PE can be attributed to the effects of the chain ends. The data indeed indicate that chain ends provide a higher diffusional fractional free volume than short chain branches. It is also possible that the effective increase in diffusivity fractional free volumes caused by methyl groups may be larger in a more constrained phase (e.g. I_{CC}) than in the liquid-like component. Von Meerwall *et al.*[40] found on studying the self-diffusion of *cis*-polyisoprene and polydimethylsiloxane that the contributions from chain ends to the free volume became substantial for samples with a molar mass less than 10^3–10^4 g mol^{-1}.

In *Figure 15*, the A parameter determined from the n-hexane desorption measurements is shown. It is reasonable to assume that A_d and B are the same for most of the samples. A change in A would then correspond to a change in the geometrical impedance expressed by the detour factor ψ. For the linear PEs, the A parameter decreases with increasing crystallinity. For the branched PEs, however, the A parameter increases with increasing crystallinity. The unexpected trend obtained for the branched PEs is in accordance with earlier data of Fleischer[4]. NR exhibited the lowest A value, which may be explained by its dissimilarity from PE showing a different A_d value. The treatment of Fricke[9,46] describing the detour factor of a system of non-penetrable oblate spheroids dispersed in a penetrable continuous matrix has been applied here to calculate the geometrical impedance of the polymers studied:

$$\psi = \left(1 + \frac{v_c[0.384 + (0.785 - L_c/w_i)^2]}{1.848 - 3(0.785 - L_c/w_i)^2}\right)^{-1} \tag{35}$$

Data for crystal width (w_i) and crystal thickness (L_c) are presented in *Table 3*. In the absence of a value for D_T^a, the detour factors were normalized with respect to the detour factor for L10, a sample that lacks a well organized superstructure. L10 exhibits a random lamellar structure. The model is admittedly approximate for the actual systems, particularly for the samples with an ordered superstructure. However, it describes fairly well the trend in the detour factor for the linear PEs. Interestingly, the model also predicts lower detour factors for B2 and B3 than for L10, in accordance with the data presented in *Figure 15*. The difference between the experimental and predicted data for the A factor for the branched PEs is substantial. The present model for polymers (equation (13)) can be compared with the original free-volume model of diffusion derived for the self-diffusion of liquids[6,7,47] using the following expression:

$$D = \frac{1}{3}\left(\frac{3RT}{M_p}\right)^{0.5} \lambda_d \exp\left(-\frac{B_d}{f}\right) \tag{36}$$

where M_p is the molar mass of the penetrant and λ_d is the step length (mean free path), which may take different values depending on the size and shape of the liquid molecule. Vogel and Weiss[47] suggested that λ_d is equal to the diameter of the liquid molecule in the case of spherical molecules. Other suggestions where the step length is a function of the fractional free volume of the system have also been made[7]. A weakness in the free-volume theory describing diffusion in polymers is that the physical meaning of the pre-exponential factor (A_d) is unknown. Kulkarni *et al.*[5] suggested that A_d is a function of the inverse of the square root of the molar mass of the penetrant, which is readily deduced from a comparison of equations (13) and (36). A further comparison leads to the following possible causes for an increasing A parameter with increasing crystallinity for branched samples: (1) the penetrant step length increases with crystallinity; (2) the B factor increases with decreasing crystallinity; (3) the PEs with low crystallinity possess a spherulitic structure which is as good as that of the high-crystallinity PEs with regard to barrier properties. The most reasonable explanation of the observed anomaly is, however, hidden in the free-volume equation (equation (13)). A small change in f_2 results in a large change in the D_T value, which then always has to be corrected for by changing the A value, i.e. the value of A is partly a result of the f_2 value obtained. At high f_2 values, A is forced to be small.

Samples L6 and B2 were immersed in liquid CCl_4 at 298.2 K in order to perform 'real-time' Raman spectroscopy analysis of PE in the presence of a solvent. CCl_4 was used since most of its Raman peaks are well separated from the peaks originating from PE. The spectra were studied in both the 'conventional' 1200–1600 cm^{-1} region and the CH_2 stretching region (2750–3000 cm^{-1}). The assessment of the I_L content was not possible due to interference between CCl_4 Raman peaks and the broad CH_2 rocking peak. The CH_2 stretching region is sensitive to small changes in both inter- and intrachain order. Owing to its high sensitivity to chain order, it has been the subject of numerous studies on paraffins and PE[48–62]. Unfortunately the spectrum in this region is complicated due to, for example, Fermi resonances, and the origins of some of the peaks are still unknown[59]. *Figure 16* shows the spectra of hexacontane and n-octadecane. The spectra of fully crystalline hexacontane and of the PE samples could be described by a series of superimposed Lorentz peaks (equation (17), $q = 2$, $k = 2846$, 2866, 2881, 2897, 2926 and 2963 cm^{-1}). The strong peaks at 2846 and 2881 cm^{-1} refer to the symmetric and antisymmetric CH_2 stretching modes respectively[63]. The 2963 cm^{-1} peak is attributed to methyl groups[48]. Note the higher intensity of this peak in the spectrum of n-octadecane compared to that of hexacontane. According to Abbate *et al.*[56], the peak at 2926 cm^{-1} is proportional to the *gauche* content; and according to Cho *et al.*[59], the broad peak at 2897 cm^{-1} corresponds to antisymmetric CH_2 stretches in mobile *trans* sequences. Cho *et al.*[59] also suggested that the sharp 2881 cm^{-1} peak is due to antisymmetric CH_2 stretch in constrained *trans* sequences. It should be mentioned that the 2926 and 2897 cm^{-1} peaks appear in the fully crystalline hexacontane, although their intensities are lower than those in fully liquid-like n-octadecane (*Figure 16*). The

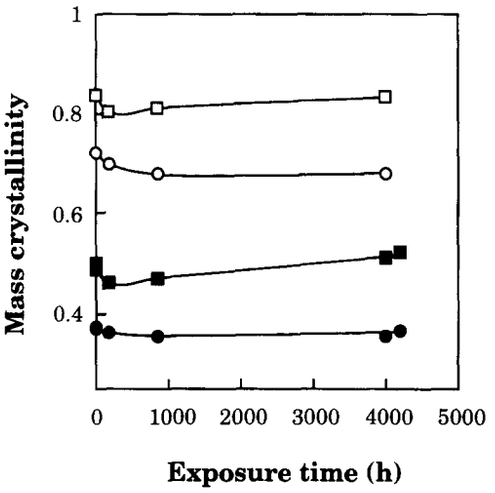

Figure 17 Crystal core (w_{CC}) (○, L6; ●, B2) and crystal core + interphase ($w_{CC} + w_{I_{CC}}$) (□, L6; ■, B2) contents as a function of CCl_4 exposure time

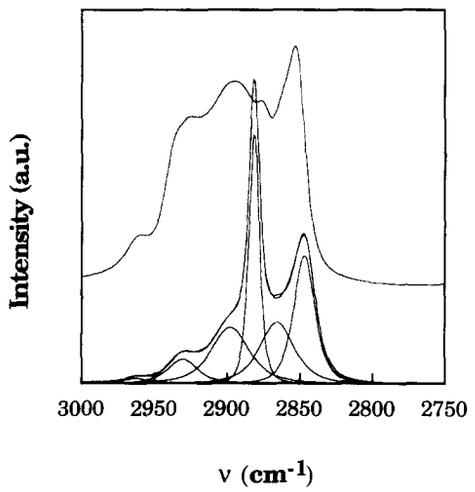

Figure 16 Raman spectra of hexacontane (lower) and n-octadecane (upper). The hexacontane spectrum is fitted with six Lorentz peaks

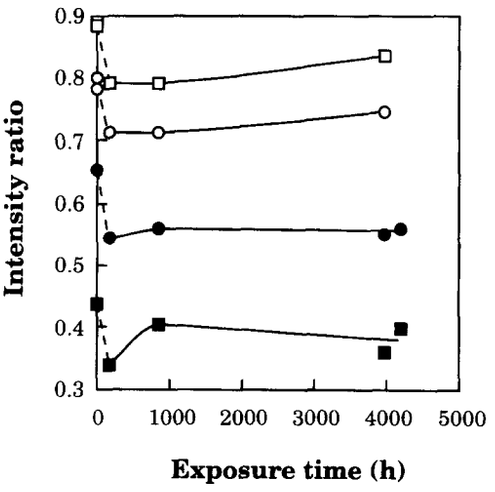

Figure 18 Intensity ratios for CCl_4-saturated L6 (○, I_{2881}/I_{2846}; □, I_{2881}/I_{2897}) and CCl_4-saturated B2 (●, I_{2881}/I_{2846}; ■, I_{2881}/I_{2897}) as a function of CCl_4 exposure time

shoulder filling the gap between 2846 and 2881 cm^{-1} is, according to Tanaka and Takemura[54], sensitive to interchain order, here described by the peak at 2866 cm^{-1}. It has also been suggested that the 2926 and 2866 cm^{-1} peaks are affected by the presence of methyl groups[54]. Richter *et al.*[60] used the peak height ratio of 2881 cm^{-1} and 2846 cm^{-1} to characterize the order in PE. From their data on the temperature dependence of the Raman spectrum, it may be concluded that this ratio is dependent on the contents of both the CC and I_{CC} components and possibly also the I_L component.

The long-term effects on the different components from CCl_4 are shown in *Figure 17*. Although the changes are small, almost within the experimental error, both linear and branched PE exhibited the same characteristic behaviour. There is an apparent decrease in the contents of both the CC and I_{CC} components followed by an increase in the I_{CC} content and possibly also in the CC content as a function of the time of exposure in CCl_4. The changes in the ratio of the integrated intensities of I_{2881} and I_{2846} peaks and the ratio of the integrated intensities of the I_{2881} and I_{2897} peaks as a function of CCl_4 exposure time are strong (*Figure 18*). The changes in both these ratios are of the same magnitude. Based on suggestions of Cho *et al.*[59], the ratio of I_{2881} to I_{2897} corresponds to the segments of less mobile *trans* sequences in the whole polymer. The data thus indicate an increase in the proportion of mobile *trans* sequences after short sorption times followed by a slow decrease in the content of mobile *trans* sequences. These processes are consonant with the observed changes in I_{CC} (and possibly also CC) contents (*Figure 17*).

CONCLUSIONS

The crystallites impose constraints on the non-crystalline chain segments in semicrystalline PE. This is reflected in the recorded high diffusivity selectivity (O_2/n-hexane) and the low fractional free volume of the non-crystalline phase.

Raman spectroscopy offers a possibility of resolving components of different conformation and mobility. From the Raman spectroscopy study, four components were resolved in PE: a crystal core (CC), a crystal-core-like interfacial (I_{CC}), a liquid-like interfacial (I_L) and a liquid component (L). The four-component approach was included in the Cohen–Turnbull–Fujita (CTF) free-volume model to describe the diffusion of n-hexane in PE. The majority of the linear and branched PEs could be described by the modified CTF model. The largest deviations occurred for low-molar-mass linear PEs. The non-crystalline phase of the low-molar-mass PEs contained mostly the I_{CC} component. The fractional free volume of this component in these samples was, however, significantly higher than in the other PE samples due to the large amount of chain ends present in the low-molar-mass PEs.

Real-time Raman spectroscopy on CCl_4-saturated PEs showed that changes in the contents of CC and I_{CC} were small during penetrant exposure.

ACKNOWLEDGEMENTS

This work has been sponsored by the Swedish Board for Technical and Industrial Development (NUTEK), Grants 89-02294P and C656109-2. The authors thank Dr S. Holding, RAPRA Technology Ltd, UK, for the s.e.c. analyses, and Professor G. Grimvall, Department of Theoretical Physics, Royal Institute of Technology, Stockholm, for valuable discussions.

REFERENCES

1 Vieth, W. R. in 'Diffusion In and Through Polymers', Hanser Verlag, Munich, 1991
2 Michaels, A. S. and Bixler, H. J. *J. Polym. Sci.* 1961, **5**, 413
3 Peterlin, A. *J. Macromol. Sci.–Phys. (B)* 1975, **28**, 57
4 Fleischer, G. *Colloid Polym. Sci.* 1984, **262**, 919
5 Kulkarni, S. S. and Stern, S. A. *J. Polym. Sci., Polym. Phys. Edn.* 1983, **21**, 441
6 Cohen, M. H. and Turnbull, D. *J. Chem. Phys.* 1959, **31**, 1164
7 Turnbull, D. and Cohen, M. H. *J. Chem. Phys.* 1970, **52**, 3038
8 Fujita, H. *Fortschr. Hochpolym. Forsch.* 1961, **3**, 1
9 Hedenvist, M., Johnsson, G., Tränkner, T. and Gedde, U. W. *Polym. Eng. Sci.* 1996, **36**, 271
10 Mutter, R., Stille, W. and Strobl, G. R. *J. Polym. Sci., Polym. Phys. Edn.* 1993, **31**, 99
11 Pasternak, R. A., Schimscheimer, J. F. and Heller, J. *J. Polym. Sci. (A-2)* 1970, **8**, 467
12 Webb, J. A., Bower, D. I., Ward, I. M. and Cardew, P. T. *J. Polym. Sci., Polym. Phys. Edn.* 1993, **31**, 743
13 Kanig, G. *Colloid Polym. Sci.* 1977, **255**, 1005
14 Olley, R. H. and Bassett, D. C. *Polymer* 1982, **23**, 1707
15 Tränkner, T., Hedenqvist, M. and Gedde, U. W. *Polym. Eng. Sci.* 1994, **34**, 1581
16 Conde Braña, M. T. and Gedde, U. W. *Polymer* 1992, **33**, 3123
17 Wunderlich, B. 'Macromolecular Physics', Vol. 1, 'Crystal Structure, Morphology and Defects', Academic Press, New York, 1973
18 Gray, A. P. *Thermochim. Acta* 1970, **1**, 563
19 Wunderlich, B. 'Macromolecular Physics', Vol. 3, 'Crystal Melting', Academic Press, New York, 1980
20 Hoffman, J. D. *Polymer* 1982, **23**, 656
21 Wunderlich, B. and Baur, H. *Adv. Polym. Sci.* 1070, **7**, 151
22 Gedde, U. W., Eklund, S. and Jansson, J.-F. *Polymer* 1983, **24**, 1532
23 Pakula, T., Kryszewski, M. and Soukup, Z. *Eur. Polym. J.* 1976, **12**, 41
24 Fels, M. and Huang, R. Y. M. *J. Appl. Polym. Sci.* 1970, **14**, 523
25 Castro, E. F., Gonzo, E. E. and Gottifredi, J. C. *J. Membr. Sci.* 1987, **31**, 235
26 Tewari, Y. B. and Schreiber, H. P. *Macromolecules* 1972, **5**, 329
27 Edsberg, L. and Wedin, P.-Å. *Optim. Meth. Softw.* in press
28 Strobl, G. R. and Hagedorn, W. *J. Polym. Sci., Polym. Phys. Edn.* 1978, **16**, 1181
29 Glotin, M. and Mandelkern, L. *Colloid Polym. Sci.* 1982, **260**, 182
30 Mandelkern, L. *Polym. J.* 1985, **17**, 337
31 Mandelkern, L. and Peacock, A. *Polym. Bull.* 1986, **16**, 529
32 Mandelkern, L., McLaughlin, K. W. and Alamo, R. G. *Macromolecules* 1992, **25**, 1440
33 Shen, C., Peacock, A. J., Alamo, R. G., Vickers, T. J., Mandelkern, L. and Mann, C. K. *Appl. Spectrosc.* 1992, **46**, 1226
34 Rull, F., Prieto, A. C., Casado, J. M., Sobron, F. and Edwards, H. G. M. *J. Raman Spectrosc.* 1993, **24**, 545
35 Naylor, C. C., Meier, R. J., Kip, B. J., Williams, K. P. J., Mason, S. M., Conroy, N. and Gerrard, D. L. F. *Macromolecules* 1995, **28**, 2969
36 Mandelkern, L. and Alamo, R. G. *Macromolecules* 1995, **28**, 2988
37 Boerio, F. J. and Koenig, J. L. *J. Chem. Phys.* 1970, **52**, 3425
38 Cheng, J., Fone, M., Reddy, V. N., Schwartz, K. B., Fischer, H. P. and Wunderlich, B. *J. Polym. Sci., Polym. Phys. Edn.* 1994, **32**, 2683
39 Kitamura, R., Horii, F. and Murayama, K. *Macromolecules* 1986, **19**, 636
40 Von Meerwall, E., Grisgsby, J., Tomich, D. and Van Antwerp, R. *J. Polym. Sci., Polym. Phys. Edn.* 1982, **20**, 1037
41 Williams, M. L., Landel, R. F. and Ferry, J. D. *J. Am. Chem. Soc.* 1955, **77**, 3701
42 Boyd, R. H. *Macromolecules* 1984, **17**, 903

43 Quinn, F. A. and Mandelkern, L. *J. Am. Chem. Soc.* 1958, **80**, 3178
44 Gordon, M. and Taylor, J. S. *J. Appl. Chem.* 1952, **2**, 493
45 Zoller, P. *J. Appl. Polym. Sci.* 1979, **23**, 1051
46 Fricke, H. *Phys. Rev.* 1924, **24**, 575
47 Vogel, H. and Weiss, A. *Ber. Bunsenges. Phys. Chem.* 1981, **85**, 539
48 Snyder, R. G., Hsu, S. L. and Krimm, S. *Spectrochim. Acta (A)* 1978, **34**, 395
49 Okabayashi, H. and Kitagawa, T. *J. Phys. Chem.* 1978, **82**, 1830
50 Snyder, R. G. and Scherer, J. R. *J. Chem. Phys.* 1979, **71**, 3221
51 Snyder, R. G., Scherer, J. R. and Gaber, B. P. *Biochim. Biophys. Acta* 1980, **601**, 47
52 Zerbi, G. and Abbate, S. *Chem. Phys. Lett.* 1981, **80**, 455
53 Abbate, S., Zerbi, G. and Wunder, S. L. *J. Chem. Phys.* 1982, **86**, 3140
54 Tanaka, H. and Takemura, T. *Japan. J. Appl. Phys.* 1983, **22**, 1001
55 MacPhail, R. A., Strauss, H. L., Snyder, R. G. and Elliger, C. A. *J. Phys. Chem.* 1984, **88**, 334
56 Abbate, S., Wunder, S. L. and Zerbi, G. *J. Phys. Chem.* 1984, **88**, 593
57 Snyder, R. G., Aljibury, A. L., Strauss, H. L., Casal, H. L., Gough, K. M. and Murphy, W. F. *J. Chem. Phys.* 1984, **81**, 5352
58 Wunder, S. L. and Merajver, S. D. *Contemp. Top. Polym. Sci.* 1984, **4**, 269
59 Cho, Y., Kobayashi, M. and Tadokoro, H. *J. Chem. Phys.* 1986, **84**, 4636
60 Richter, A., Hölzer, W., Schröter, O. and Dalcolmo, H. J. *Acta Polym.* 1991, **42**, 337
61 Del Zoppo, M. and Zerbi, G. *Polymer* 1992, **33**, 4667
62 Agosti, E., Zerbi, G. and Ward, I. M. *Polymer* 1992, **33**, 4219
63 Bower, D. I. and Maddams, W. F. in 'The Vibrational Spectroscopy of Polymers', Cambridge University Press, Cambridge, 1989
64 Bakhouya, A., El Brouzi, A., Bouzon, J. and Vergnaud, J. M. *Plast. Rubber Compos. Process. Appl.* 1993, **19**, 77

APPENDIX

Modelling desorption

In the numerical treatment of equation (8), dimensionless variables were used. The normalized volume fraction is $V_1 = v_1/v_1^\circ$ and the dimensionless space coordinate is $X = x/L$, where v_1° and L are respectively the saturation volume fraction and half the plate thickness. Dimensionless time (T_d) is defined as:

$$T_d = \frac{D_{T(v_1^a \to 0)} t}{L^2} \tag{A1}$$

Using equations (9) and (10), equation (8) can then be written in dimensionless form:

$$\frac{\partial V_1}{\partial T_d} = \frac{\partial}{\partial X}\left((1 - v_1^\circ V_1^a)(1 - 2\chi v_1^\circ V_1^a) D_T^*(v_1^\circ V_1^a)\frac{\partial V_1}{\partial X}\right) \tag{A2}$$

The right-hand side of equation (A2) used in the implicit method is discretized according to the following central difference scheme:

$$\frac{1}{\Delta X^2}\left(\zeta_{i+\frac{1}{2}} - \zeta_{i-\frac{1}{2}}\right) \tag{A3}$$

where index i denotes the integer number of the radial position and

$$\zeta_{i+\frac{1}{2}} = \left(1 - v_1^\circ V^a_{1,i+\frac{1}{2},j}\right)\left(1 - 2\chi v_1^\circ V^a_{1,i+\frac{1}{2},j}\right) \exp\left(\frac{B_d[(f_1 - f_2)v_1^\circ V^a_{1,i+\frac{1}{2},j}]}{f_2[f_2 + (f_1 - f_2)v_1^\circ V^a_{1,i+\frac{1}{2},j}]}\right)(v_{1,i+1,j} - V_{1,i,j}) \tag{A4}$$

where

$$V^a_{1,i+\frac{1}{2},j} = (V^a_{1,i+1,j} + V^a_{1,i,j})/2 \tag{A5}$$

Index j denotes time steps. Because of plate symmetry, only half the plate cross-section is analysed and the inner boundary is treated as an isolated point using central differences:

$$\left(\frac{\partial V_1}{\partial X}\right)_{X=1} = 0 \quad \Rightarrow \quad V_{1,n+1,j} = V_{1,n-1,j} \tag{A6}$$

where n is at the symmetry line. At the surface of the place, evaporation of the solute takes place:

$$(1 - v_1^\circ V_1^a)(1 - 2\chi v_1^\circ V_1^a)\frac{D_{T(v_1^a \to 0)} D_T^*(v_1^\circ V_1^a)}{L}\left(\frac{\partial V_1}{\partial X}\right)_{X=0} = F_0 V_1 \tag{A7}$$

The rate of evaporation (F_0) is determined for each sample through a procedure described in ref. 64 and a value of $2.45(\pm 0.74) \times 10^{-5}$ cm s^{-1} was obtained for F_0. The boundary condition (A7) was approximated through two different approaches ((A8)–(A11) and (A12)–(A13)). Both were compared and gave roughly the same result.

The boundary condition may be written as follows, where the surface coordinate is denoted 0:

$$V_{1,0,j} = \frac{V_{1,1,j}}{1 + N} \tag{A8}$$

where

$$N = \frac{F_0 L \Delta X}{\left(1 - v_1^\circ V^a_{1,\frac{1}{2},j}\right)\left(1 - 2\chi v_1^\circ V^a_{1,\frac{1}{2},j}\right) D_{T(v_1^a \to 0)} D_T^*\left(V^a_{1,\frac{1}{2},j}\right)} \tag{A9}$$

$$V^a_{1,\frac{1}{2},j} = (V^a_{1,0,j^*} + V^a_{1,1,j})/2 \tag{A10}$$

$$V^a_{1,0,j^*} = V^a_{1,0,j-1} + \Delta t \frac{\partial V^a_{1,1,j}}{\partial t} \tag{A11}$$

The $V^a_{1,0,j^*}$ value may also be estimated by splining along the concentration gradient. The boundary condition may also be written using a central difference:

$$V_{1,-1,j} = \frac{1 - NN}{1 + NN} V_{1,1,j} \tag{A12}$$

where

$$NN = \frac{F_0 L \Delta X}{(1 - v_1^\circ V^a_{1,0,j})(1 - 2\chi v_1^\circ V^a_{1,0,j}) D_{T(v_1^a \to 0)} D_T^*(V^a_{1,0,j})} \tag{A13}$$

NOTATION

$f_2^{I_{CC}}$	crystal-like interphase fractional free volume
$f_2^{I_L}$	liquid-like interphase fractional free volume
v_1^p	pore solute volume fraction
D_T^*	concentration-dependent term in equation (14)
$f_2^{I^*}$	corrected interphase fractional free volume

T_m°	equilibrium melting point
f^I	fractional free volume of the mixture of interphase and solute
f^L	fractional free volume of the mixture of liquid-like phase and solute
Δh_f°	heat of fusion for 100% crystalline polymer
I^p	intensity peak height
f_2^I	interphase fractional free volume
f_2^L	liquid-phase fractional free volume
$\overline{V}_1$	normalized average solute volume fraction
V_1	normalized solute volume fraction
v_1°	solute volume fraction at equilibrium sorption
$(v_1^I)^\circ$	solute volume fraction sorbed in the interphase
$(v_1^L)^\circ$	solute volume fraction sorbed in the liquid phase
$D_{T(v_1^a \to 0)}$	thermodynamic diffusion coefficient at zero solute concentration
D_T^a	thermodynamic diffusion coefficient of the non-crystalline phase
v_1^T	total solute volume fraction
v_2^I	volume fraction of the interphase in the mixture of interphase and liquid phase
$(v_2^I)^\circ$	volume fraction of the interphase in the mixture of interphase and solute
v_2^L	volume fraction of the liquid phase in the mixture of interphase and liquid phase
$(v_2^L)^\circ$	volume fraction and liquid polymer phase in the mixture of polymer liquid phase and solute
$v_{1,2}^a$	volume fractions of solute (1) and polymer (2) confined to the part outside the crystal core
$\langle L_a \rangle$	average non-crystalline interlayer thickness (from TEM)
$\langle L_c \rangle$	average crystal thickness (from TEM)
a_1	activity of penetrant
A_d	free-volume parameter
a_k	spectral peak width at half the peak height
B	blocking factor
B_d	free-volume parameter
χ	interaction parameter for the semicrystalline polymer
c_{pa}	specific heat of liquid-like component
c_{pc}	specific heat of crystal-core component
D	diffusion coefficient
D_a	diffusion coefficient of the amorphous phase
D_m	mutual diffusion coefficient
D_T	thermodynamic diffusion coefficient
f_1	fractional free volume of the solute
f_2	fractional free volume of the polymer
f^a (or f)	fractional free volume of the non-crystalline phase
F_0	rate of evaporation
h	step length along the spatial direction
I	intensity
i	integer number of the spatial position
j	integer number of the time position
K_p	pore solute-loss rate constant
L	thickness of half of the plate
l	plate thickness
λ	wavelength of light
L_a	thickness of the non-crystalline interlayer
L_c	crystal thickness
M_p	mass of penetrant molecule
n	number of x coordinates
ν	wavenumber
N_R	refractive index
p	pressure
θ, θ_i	spectral peak position
Q	flow rate of penetrant
θ_{max}	scattering angle at intensity maximum
Q_∞	steady-state flow rate of penetrant
R	the gas constant
ρ_1	solute density
ρ_2	polymer density
ρ_{CC}	crystal-core density
ρ_I	interphase density ($I_{CC} + I_L$)
ρ_L	liquid-like phase density
σ	fold surface free energy
SR	spherulite radius
T	temperature
t	time
T_1	arbitrary temperature below the melting range
T_d	dimensionless time
T_g	glass transition temperature
T_m	melting point
$v_{1,2}$	volume fractions of solute (1) and polymer (2)
v_{CC}	volume fraction of crystal core
w_{CC}	mass fraction of crystal core
w_D	mass crystallinity determined by density measurements
w_{DSC}	mass crystallinity determined by d.s.c.
w_i	crystal width
w_{ICC}	mass fraction of crystal-like interphase
w_{I_L}	mass fraction of liquid-like interphase
w_L	mass fraction of liquid-like phase
w_{NMR}	mass crystallinity determined by ^{13}C CP/MAS n.m.r.
w_{TEM}	mass crystallinity determined by TEM
X	dimensionless space coordinate
x	space coordinate
X_{et}	mole per cent of ethyl branches
ψ	detour factor
ζ	parameter in the numerical treatment of the right-hand side of equation (8)
Δh_f	heat of fusion